The JCMT Gould Belt Survey: SCUBA-2 observations of circumstellar discs in L 1495

Buckle, J.V.; Drabek-Maunder, E.; Greaves, J.; Richer, J.S.; Matthews, B.C.; Johnstone, D.; ... ; Zhu, M.

Monthly Notices
of the
ROYAL ASTRONOMICAL SOCIETY

MNRAS **449,** 2472–2488 (2015) doi:10.1093/mnras/stv438

The JCMT Gould Belt Survey: SCUBA-2 observations of circumstellar discs in L 1495

J. V. Buckle,[1,2]★ E. Drabek-Maunder,[3] J. Greaves,[4] J. S. Richer,[1,2] B.C. Matthews,[5,6] D. Johnstone,[5,6,7] H. Kirk,[5] S. F. Beaulieu,[8] D. S. Berry,[7] H. Broekhoven-Fiene,[6] M. J. Currie,[7] M. Fich,[8] J. Hatchell,[9] T. Jenness,[7,10] J. C. Mottram,[11] D. Nutter,[12] K. Pattle,[13] J. E. Pineda,[14,15] C. Salji,[1,2]† S. Tisi,[8] J. Di Francesco,[5,6] M. R. Hogerheijde,[11] D. Ward-Thompson,[13] P. Bastien,[16] H. Butner,[17] M. Chen,[6] A. Chrysostomou,[18] S. Coude,[16] C. J. Davis,[19] A. Duarte-Cabral,[9] P. Friberg,[7] R. Friesen,[20] G. A. Fuller,[15] S. Graves,[7] J. Gregson,[21,22] W. Holland,[23,24] G. Joncas,[25] J. M. Kirk,[13] L. B. G. Knee,[5] S. Mairs,[6] K. Marsh,[12] G. Moriarty-Schieven,[5] J. Rawlings,[26] E. Rosolowsky,[27] D. Rumble,[9] S. Sadavoy,[28] H. Thomas,[7] N. Tothill,[29] S. Viti,[30] G. J. White,[21,22] C. D. Wilson,[31] J. Wouterloot,[7] J. Yates[26] and M. Zhu[32]

Affiliations are listed at the end of the paper

Accepted 2015 February 24. Received 2015 February 24; in original form 2014 October 6

ABSTRACT

We present 850 and 450 μm data from the James Clerk Maxwell Telescope (JCMT) Gould Belt Survey obtained with Submillimetre Common-User Bolometer Array 2 (SCUBA-2) and characterize the dust attributes of Class I, Class II and Class III disc sources in L 1495. We detect 23 per cent of the sample at both wavelengths, with the detection rate decreasing through the Classes from I to III. The median disc mask is 1.6×10^{-3} $M_{\odot}$, and only 7 per cent of Class II sources have disc masses larger than 20 Jupiter masses. We detect a higher proportion of discs towards sources with stellar hosts of spectral type K than spectral type M. Class II discs with single stellar hosts of spectral type K have higher masses than those of spectral type M, supporting the hypothesis that higher mass stars have more massive discs. Variations in disc masses calculated at the two wavelengths suggest that there may be differences in dust opacity and/or dust temperature between discs with hosts of spectral types K to those with spectral type M.

Key words: stars: formation – stars: low mass – submillimetre: ISM.

1 INTRODUCTION

One of the fundamental properties of circumstellar discs, particularly in relation to planet formation, is their mass (Andrews et al. 2013). The most useful diagnostic of disc mass is the brightness of dust continuum emission at submillimetre wavelengths, where the dust emission is optically thin over much of the disc volume, and is not overly dependent on temperature. Disc masses are thought to decrease during the evolutionary process, either through internal processes, or due to interactions with nearby massive stars.

The traditional classification of pre-main-sequence (PMS) sources is defined observationally through the Class I–III phases (Adams, Lada & Shu 1987; Lada 1987). Class I sources are more evolved embedded young stellar objects (YSOs) with massive accretion discs, while Class II sources are T Tauri stars with gas-rich circumstellar discs where the supply of envelope material has dissipated. Class III sources are stars with tenuous or debris discs, where at least the inner part of the disc has been evacuated. The bulk of disc mass is accreted during the earliest embedded phases, but more evolved sources continue to accrete material on to the disc and stellar host. There is not always a clear distinction between Class I and Class II sources, with detailed modelling demonstrating

★ E-mail: j.buckle@mrao.cam.ac.uk
†Current address: Institute for Astronomy, ETH Zurich, Wolfgang-Pauli-Strasse 27, CH-8093 Zurich, Switzerland.

that embedded Class I sources observed face-on can be classified as Class II, while Class II discs observed edge-on may look like there is still a significant amount of envelope material remaining, and be classified as Class I (Whitney et al. 2003; Crapsi et al. 2008; Evans et al. 2009).

1.1 JCMT GBS

The Gould Belt Survey (GBS; Ward-Thompson et al. 2007) has been awarded 612 h of time on the James Clerk Maxwell Telescope (JCMT) to survey nearby star-forming regions (within 500 pc), using Heterodyne Array Receiver Programme (HARP; Buckle et al. 2009) and Submillimetre Common-User Bolometer Array 2 (SCUBA-2; Holland, Bintley & Chapin 2013). The GBS will trace the very earliest stages of star formation, providing an inventory of all the protostellar objects contained in the nearby molecular clouds of the Gould Belt, covering $\sim$700 deg^2. The key science goals of the SCUBA-2 Survey are as follows.

(i) To calculate the duration of each of the protostellar stages.
(ii) To elucidate the nature of the evolution of protostellar collapse.
(iii) To discover the origin of the initial mass function of stars, from intermediate-mass stars to substellar objects.
(iv) To discern the connection between protostars and the molecular cloud structure from which they formed.

1.2 Taurus

The Taurus star-forming complex is young, with typical YSO ages of $\sim$1 Myr (Kenyon & Hartmann 1995). As a result, even its most evolved sources may have remnants of dusty discs surrounding them, since low-mass stars have a median disc lifetime of a few Myr (Williams & Cieza 2011). This is one of the key reference regions for the distribution of disc masses (Andrews & Williams 2005; Andrews et al. 2013). It is well studied, nearby, and contains some of the most complete and well-characterized catalogues of disc sources (e.g. Luhman et al. 2010; Furlan et al. 2011; Esplin, Luhman & Mamajek 2014). The complex has a significant population of YSOs that have no remaining envelope, exposing the disc and the lack of Class 0 sources provides evidence that even the embedded sources are reasonably evolved. The observations of L 1495 presented here probe dust continuum emission which spans protostellar evolutionary phases. Moreover, the wide-field mapping shown here ensures disc parameters can be examined without selection bias when examining source statistics, something shown to be problematic for previous snapshot surveys (Andrews et al. 2013).

The low stellar density in Taurus (1–10 stars pc^{-2}; Gomez et al. 1993; Güdel, Padgett & Dougados 2007), with the most massive star in L 1495 an intermediate Ae star, suggests that disc evolution is expected to proceed through dynamical star–disc or, in multiple systems, by disc–disc interactions, rather than evaporation by radiation from nearby stars. Recent observations (Lee, Williams & Cieza 2012; Dodds et al. 2015) indicate that the eventual primitive planetary systems that are the end results of disc evolution may be dependent on the natal environment, a topic which can be investigated using the large-scale maps obtained by the GBS.

One of the most direct measures of planet-forming capability in discs is the mass that they contain. The submillimetre regime, where thermal dust emission is optically thin throughout the disc, provides one of the best methods of inferring disc mass. At these wavelengths, observations are sensitive to micron- to millimetre-sized grains. With grain growth and dust settling expected to occur in the inner disc, where temperatures are warmer, submillimetre observations are able to trace the mass in discs to later evolutionary phases than infrared observations can (Hernández et al. 2007; Ricci et al. 2010). With dual-wavelength observations of all the Class I, II and III sources in L 1495, we are able to assess the effects of temperature and dust opacity on measurements of disc mass in a consistent manner.

Section 2 describes the observations, data reduction and processing and disc sample. We present analyses of the physical characteristics of the discs in Section 3, and discuss disc evolution in Section 4. Finally, in Section 5 we summarize the conclusions of this research.

2 OBSERVATIONS

The SCUBA-2 (Holland et al. 2013) observations presented here form part of the JCMT Gould Belt Survey (GBS; Ward-Thompson et al. 2007). Continuum observations at 850 and 450 μm were made using fully sampled 30-arcmin diameter circular regions (PONG1800 mapping mode; Chapin et al. 2013). Also included are observations from the GBS Science verification phase, taken in PONG900 and PONG3600 mapping modes. Larger regions were mosaicked with overlapping scans.

The data were reduced using an iterative map-making technique (makemap in SMURF; Chapin et al. 2013), and gridded to 6 arcsec pixels at 850 μm and 4 arcsec pixels at 450 μm. The iterations were halted when the map pixels, on average, changed by $<$0.1 per cent of the estimated map rms. The initial reductions of each individual scan were co-added to form a mosaic from which a signal-to-noise mask was produced for each region. The final mosaic was produced from a second reduction using this mask to define areas of emission, with individual scans cropped to exclude noisy edge regions.

Detection of emission structure smaller in size than the spatial filter are robust both inside and outside of the masked regions. A spatial filter of 600 arcsec is used in the reduction, and tests with simulated data show that flux recovery is robust for sources with a Gaussian full width at half-maximum (FWHM) less than 2.5 arcmin, provided that the source peak brightness is several times the noise. Sources between 2.5 and 7.5 arcmin will be detected, but both the flux and the size are underestimated because Fourier components with scales greater than 5 arcmin are removed by the filtering process. Detection of sources larger than 7.5 arcmin is dependent on the mask used for reduction. In this analysis, we focus on compact disc sources, which, even with their remnant envelopes, have size scales $<$1 arcmin (0.04 pc at a distance of 140 pc), where we expect flux recovery to be robust at both 850 and 450 μm.

The data are calibrated in mJy pixel^{-1}, using aperture flux correction factors (FCFs) of 2.34 and 4.71 Jy pW^{-1} arcsec^{-2} at 850 and 450 μm, respectively, derived from average values of JCMT calibrators (Dempsey et al. 2013), and correcting for the pixel area. The PONG scan pattern leads to lower noise in the map centre and overlap regions, while data reduction and emission artefacts can lead to small variations in the noise over the whole map.

Fig. 1 shows the calibrated emission maps at 850 and 450 μm on the left, and the error maps on the right, which are also contoured with the mask used for data reduction. A mean 1σ uncertainty of 1.7 mJy pixel^{-1} at 850 μm was achieved in the final L 1495 mosaic. The inclusion of science verification data leads to a variation in noise across the final mosaic, due to the differences in spatial coverage. We achieve a better, more consistent sensitivity within the masked regions, however. Within the masked region, which is the focus of

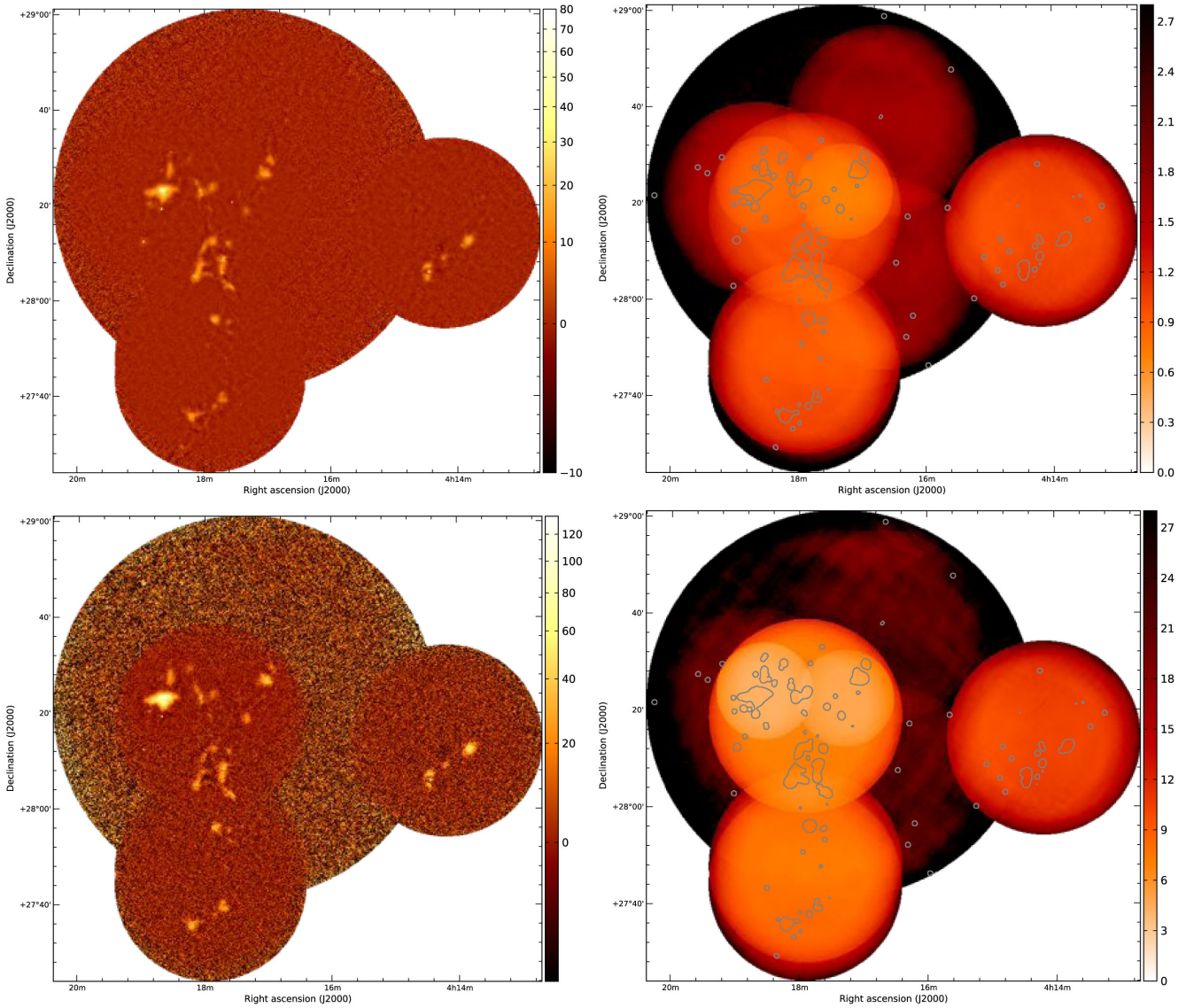

Figure 1. SCUBA-2 850-μm (top) and 450-μm (bottom) continuum images (left) and error maps (right) of L1495. Fluxes are in mJy pixel^{-1}. Contours on the error maps show the mask used in the data reduction (Section 2). Note that the data maps are on a logarithmic colour scale, while the error maps are on a linear scale, with the colour-coding reversed.

the science presented here, a mean 1σ rms of 0.98 mJy pixel^{-1}, equivalent to 2.5 mJy beam^{-1}, was achieved. For the 450 μm data, a mean 1σ rms of 5.1 mJy pixel^{-1}, equivalent to 13.3 mJy beam^{-1}, was achieved inside the masked region.

2.1 Disc sources in L 1495

We use the most comprehensive disc catalogues of Taurus (Luhman et al. 2010; Esplin et al. 2014) to identify Class I, Class II and Class III sources in L 1495, which are listed in Table 1. We have applied updated spectral types published by Herczeg & Hillenbrand (2014) and Pecaut & Mamajek (2013), as well as details of multiplicity of PMS stars in Taurus (e.g. Akeson & Jensen 2014) and the classification of sources as transition discs (e.g. Najita, Strom & Muzerolle 2007; Furlan et al. 2011). Note that there are no known Class 0 sources in this region. Figs A1–A56 in Appendix A show thumbnail continuum images of all the discs in our sample.

2.2 CO contamination of dust continuum

Dust continuum measurements in the submillimetre, observed using wide-band filters, can be contaminated by flux from molecular lines. Lines of ^{12}CO are particularly problematic, as they are the brightest lines in the submillimetre wavelength range. For SCUBA-2, the ^{12}CO $J = 3$–2 transition is near the central transmission peak of the 850-μm bandpass filter, and can dominate dust continuum observations in regions of energetic molecular outflow (Drabek et al. 2012). The JCMT GBS data sets include large-scale molecular line maps in ^{12}CO $J = 3$–2, which we utilize, following the techniques described in Drabek et al. (2012) to quantify the contribution of ^{12}CO emission to our dust continuum measurements.

We use the JCMT GBS HARP observations of Taurus (Davis et al. 2010), which comprise CO $J = 3$–2 maps along the northwest region of Taurus known as L 1495. The region contains a diffuse cloud (named as a bowl or hub; Davis et al. 2010) which is the focus of the dust continuum observations presented here. The

Table 1. Background-subtracted continuum flux measurements, from aperture photometry, with 1σ uncertainties on the mean and integrated fluxes, which do not include the calibration errors. Sources are ordered by class, then right ascension, with names, class and spectral types as given in the catalogues (Luhman et al. 2010; Esplin et al. 2014).

No.[a]	ID	Class	Sp.type	Mean F_{850} (mJy pixel^{-1})	Total F_{850} (mJy)	Mean F_{450} (mJy pixel^{-1})	Total F_{450} (mJy)	Per cent CO
1	J04153566+2847417	I	–	2.85 ± 1.17	25.7 ± 10.6	4.25 ± 7.16	82.9 ± 140	N/O
2	SSTTau041831p2+28261	I	–	3.40 ± 0.36	30.7 ± 3.27	6.20 ± 1.32	120 ± 26	<5
3	IRAS 04108+2803B	I	K0	5.91 ± 0.44	53.3 ± 4.01	14.8 ± 3.14	288 ± 61.6	<5
4	IRAS 04111+2800G	I	K0	4.60 ± 0.50	41.5 ± 4.54	11.0 ± 2.94	215 ± 57.8	13
5	IRAS 04108+2803A	I	M4.75	4.63 ± 0.44	41.8 ± 3.99	14.7 ± 3.14	287 ± 61.6	<5
6	IRAS 04154+2823	I	M2.5	7.20 ± 0.43	65.0 ± 3.89	11.3 ± 1.37	221 ± 26.9	N/O
7	CoKuTau/1	I	M0	1.91 ± 0.40	17.3 ± 3.64	4.58 ± 1.25	89.3 ± 24.6	8
8	IRAS 04158p2805	I	M5.25	22.3 ± 0.46	201 ± 4.15	56.7 ± 2.24	1110 ± 44.0	<5
9	V410X-ray7	II	M0.75	1.38 ± 0.36	12.5 ± 3.27	2.61 ± 1.37	50.9 ± 27.0	<5
10	J04141188+2811535	II	M6.25	0.94 ± 0.44	8.50 ± 3.96	-3.84 ± 3.13	-74.9 ± 61.6	<5
11	V773 Tau A+B	II^{T}	K3	1.23 ± 0.44	11.1 ± 3.96	-6.02 ± 3.14	-117 ± 61.7	<5
12	FM Tau	II	M4.5	1.19 ± 0.48	10.8 ± 4.37	-2.17 ± 2.88	-42.3 ± 56.5	<5
13	FN Tau	II	M3.5	1.62 ± 0.53	14.7 ± 4.78	8.07 ± 3.11	158 ± 61.0	N/O
14	CW Tau	II	K3.0	6.55 ± 0.49	59.2 ± 4.41	16.9 ± 2.90	330 ± 57.0	<5
15	CIDA1	II	M4.5	0.39 ± 0.50	3.56 ± 4.58	4.59 ± 2.99	89.6 ± 58.6	<5
16	MHO1/2	II	M2.5	48.9 ± 0.46	442 ± 4.20	85.7 ± 3.03	1670 ± 59.5	<5
17	MHO3	II	M2.2	2.02 ± 0.51	18.3 ± 4.62	2.30 ± 3.03	44.8 ± 59.6	10
18	FO Tau A+B	II^{T}	M3.9	1.80 ± 0.46	16.2 ± 4.20	7.82 ± 2.73	153 ± 53.5	N/O
19	J04153916+2818586	II	M4.0	1.64 ± 0.78	14.8 ± 7.04	1.36 ± 5.59	26.5 ± 110	<5
20	J04155799+2746175	II	M5.2	2.31 ± 2.02	20.8 ± 18.3	13.9 ± 11.1	271 ± 217	N/O
21	J04161210+2756385	II	M4.75	−0.28 ± 0.84	−2.54 ± 7.66	−6.06 ± 6.04	−118 ± 119	N/O
22	J04163911+2858491	II	M5.5	−0.33 ± 1.90	−3.02 ± 17.20	3.82 ± 7.01	74.6 ± 137	N/O
23	CY Tau	II	M2.3	13.7 ± 0.30	124 ± 2.68	10.0 ± 1.38	196 ± 27.0	<5
24	KPNO10	II	M5	2.21 ± 0.44	20.0 ± 4.03	−1.35 ± 1.94	−26.3 ± 38.1	<5
25	V410X-ray1	II	M3.7	−0.12 ± 0.45	−1.06 ± 4.09	−0.03 ± 1.99	−0.60 ± 39.0	N/O
26	V410Anon13	II	M5.75	−0.68 ± 0.41	−6.16 ± 3.75	−0.01 ± 1.31	−0.28 ± 25.7	N/O
27	DD Tau A+B	II	M4.8	2.10 ± 0.38	19.0 ± 3.41	6.17 ± 1.43	121 ± 28.1	<5
28	CZ Tau A+B	II	M4.2	−0.06 ± 0.37	−0.56 ± 3.38	−0.77 ± 1.43	−15.0 ± 28.0	<5
29	V410 X-Ray 2	II	M0	1.25 ± 0.42	11.3 ± 3.84	0.59 ± 1.31	11.6 ± 25.8	N/O
30	V892 Tau	II	A0	43.3 ± 0.34	391 ± 3.06	74.3 ± 1.24	1450 ± 24.3	<5
31	LR 1	II	K4.5	3.05 ± 0.40	27.5 ± 3.65	11.7 ± 1.23	229 ± 24.1	13
32	V410 X-Ray 6	II^{T}	M5.9	1.10 ± 0.43	9.90 ± 3.94	3.53 ± 1.44	68.9 ± 28.3	9
33	KPNO12	II	M9	0.33 ± 0.97	2.96 ± 8.77	4.25 ± 6.18	82.9 ± 121	N/O
34	FQ Tau A+B	II^{T}	M4.3	−0.31 ± 0.74	−2.77 ± 6.73	0.70 ± 5.60	13.6 ± 110	N/O
35	V819 Tau	II^{T}	K8.0	−0.33 ± 0.75	−2.94 ± 6.83	10.4 ± 5.68	203 ± 112	N/O
36	FR Tau	II	M5.3	0.25 ± 0.77	2.26 ± 6.98	4.22 ± 5.59	82.4 ± 110	N/O
37	J04201611+2821325	II	M6.5	3.83 ± 2.33	34.6 ± 21.1	2.39 ± 12.1	46.6 ± 238	N/O
38	LkCa1	III	M4	−0.26 ± 0.51	−2.38 ± 4.64	−2.70 ± 3.10	−52.7 ± 60.8	<5
39	Anon1	III	M0	−0.64 ± 0.48	−5.74 ± 4.37	0.90 ± 2.93	17.5 ± 57.5	<5
40	XEST20-066	III	M5.2	0.42 ± 0.54	3.77 ± 4.87	−4.96 ± 3.01	−96.8 ± 59.0	<5
41	XEST20-071	III	M3.1	1.34 ± 0.48	12.1 ± 4.38	0.02 ± 2.81	0.42 ± 55.1	<5
42	CIDA2	III	M5.5	0.63 ± 0.48	5.71 ± 4.34	−0.33 ± 2.79	−6.35 ± 54.7	<5
43	KPNO1	III	M8.5	0.10 ± 0.91	0.93 ± 8.27	0.53 ± 5.37	10.3 ± 106	N/O
44	J04161885+2752155	III	M6.25	−0.79 ± 0.82	−7.17 ± 7.43	3.89 ± 5.93	75.9 ± 116.3	N/O
45	LkCa4	III	M1.3	1.03 ± 0.81	9.32 ± 7.37	16.0 ± 6.21	312 ± 122	N/O
46	LkCa5	III	M2.2	−0.54 ± 0.48	−4.91 ± 4.32	−3.85 ± 2.10	−75.2 ± 41.3	N/O
47	V410Xray3	III	M6.5	−0.87 ± 0.41	−7.88 ± 3.69	−1.74 ± 1.30	−33.9 ± 25.6	<5
48	V410Anon25	III	M1	1.68 ± 0.36	15.18 ± 3.26	1.81 ± 1.32	35.4 ± 25.9	<5
49	KPNO11	III	M5.9	−0.08 ± 0.47	−0.68 ± 4.28	0.54 ± 2.23	10.5 ± 43.8	N/O
50	V410 Tau A+B+C	III	K7	0.43 ± 0.40	3.91 ± 3.59	−0.24 ± 1.24	−4.76 ± 24.3	<5
51	V410X-ray4	III	M4	1.94 ± 0.39	17.50 ± 3.58	−0.98 ± 1.21	−19.2 ± 23.8	<5
52	Hubble4	III	K8.5	−0.17 ± 0.40	−1.52 ± 3.59	0.61 ± 1.24	12.0 ± 24.3	<5
53	KPNO2	III	M7.5	0.49 ± 0.46	4.46 ± 4.21	−4.92 ± 1.94	−96.0 ± 38.1	<5
54	V410X-ray5a	III	M5.5	−0.17 ± 0.43	−1.50 ± 3.95	−0.93 ± 1.41	−18.1 ± 27.7	N/O
55	J04144158+2809583	III	–	0.94 ± 0.48	8.45 ± 4.33	0.56 ± 2.81	10.9 ± 55.1	<5
56	J04161726+2817128	III	–	1.26 ± 0.80	11.4 ± 7.28	0.78 ± 6.03	15.1 ± 118	<5

Notes. [a]850-μm detected sources are indicated in boldface, and underlined if also detected at 450 μm.
[T]Identifies a transition disc.

CO data were processed through the same iterative map maker as the 850 μm data, to apply the same spatial filtering (Hatchell et al. 2013; Sadavoy et al. 2013).

In the quiescent Taurus region, emission from CO is relatively diffuse, with only a few locations of strong emission, associated with high-velocity protostellar outflows (Davis et al. 2010). The level of CO contamination does not exceed 15 per cent, the 850-μm systematic flux uncertainty, and is generally below 5 per cent, as shown in Table 1 for the disc sources in our sample. Sources not detected at 850 μm are marked as '–', while sources which were not observed in ^{12}CO are marked as 'N/O' in the table. The results are consistent with results from other clouds (e.g. Drabek et al. 2012), where high levels of CO contamination in the 850-μm dust continuum emission are associated with energetic molecular outflows. Such outflows are rarer in the L 1495 region observed here, which is more evolved than other parts of Taurus (Davis et al. 2010). Of the two Class I and three Class II disc sources with CO contamination levels >5 per cent, IRAS 04111+2800G (Class I) drives a high-velocity outflow, while CoKu Tau 1 (Class I), MHO3 (Class II) and V410 X-ray 6 (Class II) are associated with high-velocity redshifted CO emission (Davis et al. 2010). The remaining Class II source with contamination >5 per cent, LR1, is a compact dust source embedded in weaker extended emission (both dust emission and CO integrated intensity) with local CO spectra having multiple velocity components.

Given the low levels of CO contamination in the 850 μm band, we do not expect any measurable contamination in the 450 μm band, where the ^{12}CO $J = 6$–5 transition lies at the edge of the SCUBA-2 bandpass filter (Drabek et al. 2012).

3 ANALYSIS

Background-subtracted mean and integrated flux densities for the disc sample were measured using 20 arcsec diameter apertures, with the background level estimated from nearby pixels in annuli between 30 and 40 arcsec. For a few crowded regions, nearby background regions with 20 arcsec diameter apertures were chosen manually. Table 1 shows the integrated flux values with 1σ uncertainties for each disc source, as well as information on the class and spectral type.

Using a detection criteria of 3σ or better in total flux, we detect 88 per cent (7/8) of the Class I sources at each wavelength. For Class II sources, we detect 38 per cent (11/29) at 850 μm and 21 per cent (6/29) at 450 μm. Only 11 per cent (2/19) of the Class III sources are detected 850 μm, and none at 450 μm. Table 2 summarizes detections at the 3σ level for all the sources, by wavelength, class, spectral type and multiplicity. As discussed in Section 2, our reduction algorithm filters out emission on scales of a few arcminutes, and so these observations are not sensitive to emission from the surrounding cloud. The presence of large remnant envelopes can increase the submillimetre continuum around disc sources, particularly for more embedded, younger sources. Removing the local background using close annuli should compensate in part for such contributions, although the results are then more likely to be affected by contamination from the error beam. We investigate the contribution of emission from surrounding envelopes and loud material in Section 3.2.

Table 2. 3σ detection statistics in percentages for the disc sources.

Category	No. of sources	Per cent Detections	
		850 μm	450 μm
All	56	36	23
I	8	88	88
II	29	38	21
III	19	11	0
Sp type K	8	50	50
Sp type M	43	33	16
Multiple	7	43	29
Single	49	35	22

The sources in our sample are dominated by discs with stellar hosts of spectral type M, which have lower detection rates than for discs with hosts of spectral type K, as previously found in studies focusing on late spectral types (Schaefer et al. 2009; Andrews et al. 2013). Several of the sources are known binary or multiple sources, and these have a slightly higher detection rates (29 and 22 per cent for multiple and single sources, respectively, at both wavelengths) than sources thought to be single systems, although there is, again, a large difference in the numbers of sources in each category. There are no known multiple Class I sources in our sample, and we do not detect the single Class III multiple source. We analyse these trends further in Section 4.

For sources that are not detected, a flux limit can be obtained from the mean and standard error on the mean of the associated integrated flux values, listed in Table 1. For Class II and III sources at 850 μm, the mean flux and standard error on the mean are 6.24 ± 2.38 and 1.55 ± 1.57 mJy, respectively. At 450 μm, the mean flux and standard error on the mean are 42.7 ± 19.7 and 5.1 ± 19.8 mJy for Classes II and III, respectively.

3.1 Physical characteristics of dust in the disc sample

A measure of the planet-forming capabilities of circumstellar discs is determining if they contain sufficient mass (>20 $M_{\rm JUP}$ of dust and gas) to create the equivalent of a primitive Solar system (Davis 2005). Accurately measuring disc masses is a vital step in understanding disc evolution and the diversity of exoplanets. The opacity of dust is known to be one of the largest uncertainties in accurately assessing disc mass (e.g. Beckwith et al. 1990). With observations at two wavelengths for our complete sample of discs we investigate the spectral slope, and through it the dust opacity and temperature, before calculating disc masses. The analyses are described in the following sections, and the results presented in Table 3. Results and calculations are all for detections at >3σ unless otherwise stated.

3.1.1 Continuum slopes

The slope (α) of the continuum submillimetre emission can be calculated from the simple spectral index:

$$\alpha = \frac{\ln(F_{450}) - \ln(F_{850})}{\ln(850) - \ln(450)} \quad (1)$$

for sources with emission detected at 3σ or greater in both wavelengths. For the disc sources, we use the integrated fluxes reported in Table 1 to calculate individual α values. For optically thin and isothermal emission, where the Rayleigh–Jeans criteria applies (e.g. dust temperatures >20 K for $h\nu > kT$ at 850 μm, and >35 K at 450 μm), then α=2+β, where β is the power-law index of the dust opacity (κ) at submillimetre wavelengths:

$$\kappa_{\nu_1} = \kappa_{\nu_2} \left(\frac{\nu_1}{\nu_2} \right)^{\beta}. \quad (2)$$

Table 3. Physical parameters derived from continuum measurements.

# ID	Class	Mass (20 K) $\times 10^{-3}$M$_\odot$	$T_{\rm dust}$ (K)	Mass ($T_{\rm dust}$) $\times 10^{-3}$M$_\odot$	α
2	I	1.69	24.5	1.27	2.69
3	I	2.94	48.9	0.91	2.36
4	I	2.29	37.6	0.98	1.80
5	I	2.31	50.0	0.70	2.91
6	I	3.59	6.96	28.0	1.38
7	I	0.95	16.8	1.24	2.92
8	I	11.1	14.6	18.3	2.32
9	II	0.69	5.47	–	–
13	II	1.05	16.1	–	–
14	II	3.26	18.2	3.78	2.47
16	II	24.4	17.3	30.3	1.73
17	II	1.01	–	–	–
18	II	0.86	–	–	–
23	II	6.84	7.55	43.3	0.43
24	II	1.10	–	–	–
27	II	1.05	16.7	1.38	2.32
30	II	21.6	12.8	44.9	1.80
31	II	1.52	32.2	0.79	2.59
48	III	0.84	–	–	–
51	III	0.97	–	–	–

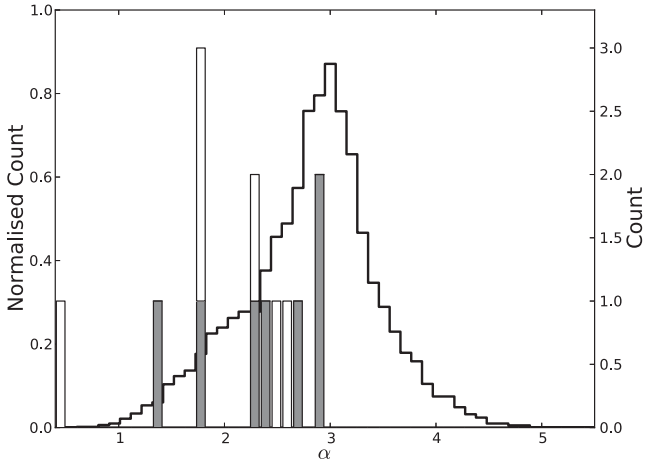

Figure 2. Normalized distribution of α values (left axis, stepped histogram) calculated from the simple spectral index (equation 1) for all pixels detected with $>3\sigma$ in the L 1495 region. Individual counts (right axis) for Class I (grey) and Class II (white) disc sources are also shown.

In this case, we expect α values of 3 if $\beta = 1.0$, as appropriate for disc sources (e.g. Beckwith et al. 1990), or tending to higher values if $\beta > 1.0$. For optically thick emission, or for dust grains much larger than the wavelength, values of $\alpha \approx 2$ are expected, regardless of β values. To ensure the same scales are sampled at both wavelengths, we use cross-convolved data sets for this, by convolving the 850 μm map with 2D Gaussians representing the primary and secondary beams at 450 μm, and similarly for the 450 μm map to produce resolution-matched maps. The FWHM of the primary/secondary beams are 7.9/13.0 arcsec and 25.0/48.0 arcsec at 450 and 850 μm, respectively. The error beam at 450 μm contributes significantly to flux in a large area (Dempsey et al. 2013), where the relative volumes of the primary and secondary beams are 0.78/0.22 at 850 μm and 0.61/0.39 at 450 μm. Fig. 2, (left axis, stepped histogram), shows the distribution of α across L 1495, obtained from all pixels in Fig. 1 with a detection $>3\sigma$. The distribution has a mean and standard deviation of 2.8 ± 0.6. Since regions with significant detections at 450 μm are compact, and generally towards star-forming cores in the L 1495 region, this distribution suggests we are tracing little of the extended cloud material, where β values of 1.5 (and $\alpha \geq 3.5$ for $\alpha = 2+\beta$) or higher may be expected.

Fig. 2 also shows the distributions of α values in the disc sources, which are similar for Class I and Class II sources. CY Tau has an anomalously low value of 0.42, although this is consistent with previously published submillimetre values (e.g. Andrews & Williams 2005). There are four sources with $\alpha > 2.5$, implying $\beta \sim 1.0$, and eight sources with $\alpha < 2.5$, implying either grain growth, or optically thick emission. Although we are not able to distinguish between these scenarios, the similar distribution we find between Class I and Class II discs provides evidence that disc evolution must be rapid. Under the assumption of optically thin, isothermal and warm (>20 K) emission from dust in the discs, these results suggest that a value of $\beta = 1.0$ is appropriate to use in the rest of the analyses presented here.

3.1.2 *Temperature*

Alternatively, the dust temperature can be inferred from the flux ratio (equation 3), given an assumed value of β:

$$\frac{F_{450}}{F_{850}} = \left(\frac{850}{450}\right)^{3+\beta} \left(\frac{\exp(hc/\lambda_{850}kT_{\rm dust}) - 1}{\exp(hc/\lambda_{450}kT_{\rm dust}) - 1}\right). \quad (3)$$

A flux ratio map was created using the cross-convolved data sets, as described in Section 3.1.1 The dust temperature map was created from the ratio map for $\beta = 1.0$, as determined in Section 3.1.1, with a high-temperature cap of 50 K, above which the flux ratio does not constrain the dust temperature (e.g. Salji et al. 2014). Fig. 3 (left axis) shows the normalized temperature distribution calculated from the flux ratio (equation 3) of the L1495 region for $\beta = 1.0$ and 1.8. A value of $\beta = 1.8$ is more appropriate for emission from the ISM, while the disc sources are more accurately described with $\beta = 1.0$. Also shown is the temperature distribution for Class I and Class II disc sources, calculated assuming $\beta = 1.0$. Although both classes have similar distributions of temperatures, the sources with the highest temperatures are all Class I. The median flux ratio for all the sources is 4.3, implying a dust temperature of 20 K if $\beta = 1.0$. The Class I sources' flux ratios extend to higher values than those

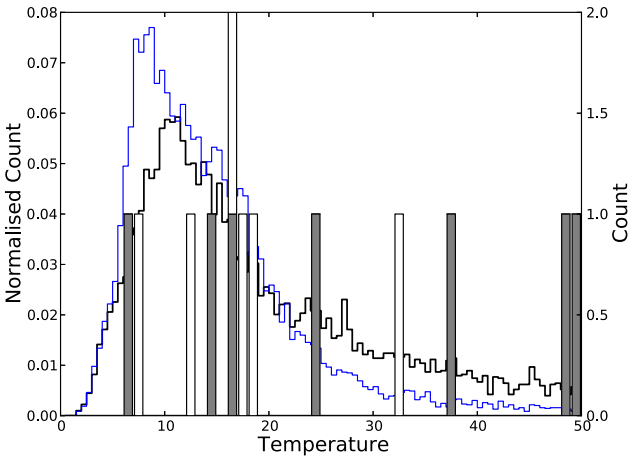

Figure 3. Normalized distribution of dust temperatures (left axis) calculated from the flux ratio map (equation 3), assuming $\beta = 1.8$ (blue) and $\beta = 1.0$ (black). Temperature counts for Class I (grey) and Class II (white) disc sources are shown on the right axis, assuming $\beta = 1.0$.

of the Class II sources, with median flux ratios of 4.6/4.0 leading to dust temperatures of 23/18 K, respectively. We are removing the local background emission in which the disc sources are embedded. However, it is possible that the envelopes may be still contributing to flux from the Class I sources. If so, this will affect the flux ratios to a larger extent than for the Class II sources. Higher 450/850 flux ratios can be due to higher dust temperatures and/or a higher opacity index β (Hatchell et al. 2013), and requires flux measurements at additional wavelengths to disentangle.

Two disc sources have $5 \leq T_{\rm dust} \leq 10$ K, while three have $30 \leq T_{\rm dust} < 50$ K, and one has a flux ratio too high to estimate the temperature reliably. Note, however, that the majority of the disc sources are in the regime where the Rayleigh–Jeans criteria fails at one or both wavelengths, and so the continuum slope is not well constrained. These sources may have contributions from surrounding material with different dust emission properties, requiring different β values, and for these sources interferometric observations will be required to isolate emission from the compact disc. The similar range of dust temperatures calculated for both classes suggests that adopting a single constant dust temperature for all sources not detected at both wavelengths will provide consistent results. A dust temperature of 20 K is consistent with the median values derived for both Class I and Class II sources, and also in line with previous work (e.g. Andrews & Williams 2005; Mohanty et al. 2013; Williams et al. 2013). We therefore adopt a constant disc temperature of 20 K in calculating disc masses for the rest of the analyses presented here.

3.1.3 *Masses*

To determine the disc mass for all of the sources detected in at least one wavelength, we use values of $T_{\rm dust} = 20$ K and $\beta = 1.0$, consistent with the above analyses. We assume that the emission is optically thin, the opacity law does not change from source to source, and can be described with a single characteristic temperature across the unresolved disc, so that the disc mass (dust + gas) scales with the observed flux density (F_ν):

$$M_{\rm d} = \frac{F_\nu D^2}{\kappa_\nu B_\nu(T_{\rm dust})}, \quad (4)$$

where D is the distance to Taurus (we adopt the canonical value of 140 pc; Elias 1978). $B_\nu(T_{\rm dust})$ is the Planck function for the given dust temperature, and κ_ν is the wavelength-dependent dust opacity. We adopt a dust opacity of $\kappa_{850} = 0.0035$ m^2 kg^{-1}, which assumes a gas-to-dust ratio of 100:1, and follows from the commonly adopted value for discs of $\kappa_{1.3\,\rm mm} = 0.0023$ m^2 kg^{-1} (e.g. Beckwith et al. 1990), with $\beta = 1$ (equation 2). Where sources were detected at both wavelengths, masses have also been calculated from the inferred dust temperature (equation 3), and these are both listed in Table 3.

Fig. 4 shows the mass distribution of the disc sources, assuming $T_{\rm dust} = 20$ K, which has a mean disc mass of 4.5×10^{-3} M$_\odot$ ($\sim$4 $M_{\rm JUP}$), and a median disc mass of 1.6×10^{-3} M$_\odot$ ($\sim$1 $M_{\rm JUP}$). The Class II sources have higher mass, on average, than the Class I sources, dominated by the bright A0 source, V892 Tau, and the multiple source MHO 1/2, both with disc masses $> 20\ M_{\rm JUP}$.

For sources where we are able to derive a dust colour temperature, the two cold sources, with $T_{\rm dust}$ <10 K, have $M(T_{\rm dust}) > 20\ M_{\rm JUP}$ (assuming $\beta = 1$). One of these, CY Tau, has been shown in recent high-resolution molecular line observations to have a compact disc, at a low inclination (Guilloteau et al. 2014). If the disc is compact, then the large mass in a small disc indicates high column densities,

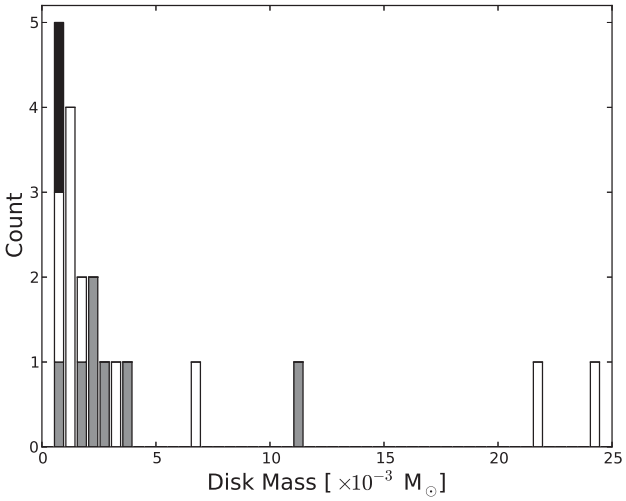

Figure 4. Mass distribution of disc sources, assuming $T_{\rm dust} = 20$ K. Classes I, II and III are shown in grey, white and black, respectively. One Jupiter mass, $M_{\rm JUP} = 1.05 \times 10^{-3}$ M$_\odot$.

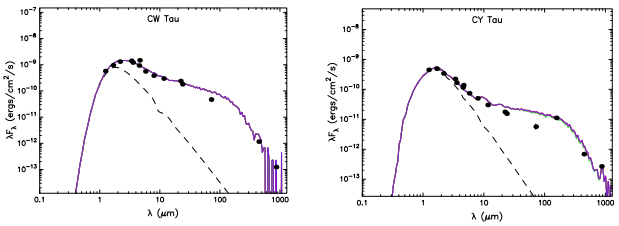

Figure 5. The filled circles show the input fluxes and the coloured lines show the best fits to the SED (Robitaille et al. 2007). The dashed line shows the stellar photosphere corresponding to the central source of the best-fitting model, as it would look in the absence of circumstellar dust (but including interstellar extinction). Disc masses derived from the best-fitting models of the SED are 7.34×10^{-3} M$_\odot$ (CW Tau) and 27.9×10^{-3} M$_\odot$ (CY Tau).

and so the assumption of optically thin dust emission may not be valid, and the disc mass underestimated.

The above analysis demonstrates that the simultaneous dual-wavelength wide-area mapping observations attainable with SCUBA-2 provide valuable constraints on the physical characteristics of the dusty circumstellar discs. To further demonstrate the validity of these results, we can compare disc masses derived above with those derived using spectral energy distribution (SED) models of YSOs. We use the web-based tools of Robitaille et al. (2007), obtaining shorter wavelength photometric data from 2MASS, IRAC and MIPS using published catalogues (Cutri et al. 2003; Roeser et al. 2008; Redbull et al. 2010; Cutri et al. 2014). The SED-fitting tool (Robitaille et al. 2007) utilizes a large grid of pre-computed models that span a wide range of parameter space in order to fit the SED, and provides the resulting model fits as data files and as SED plots, shown in Fig. 5 for two of the sources detected at both wavelengths, CY Tau and CW Tau. The SCUBA-2 observations suggest that CY Tau has a more massive disc than CW Tau, which results from SED-fitting support. The masses derived from SCUBA-2 observations, and those derived from SED fitting, agree to within a factor of 2 for both sources.

We are also able to calculate masses from the 450 μm flux, which should be similar to the masses derived from 850 μm fluxes, if our assumptions on the dust opacity index (equation 2) are correct and extend to 450 μm. For a constant dust temperature of 20 K, the mean

and standard error of the M_{450}/M_{850} ratio is 1.16 ± 0.11. The lower mass discs have the largest variation in the mass ratio, but differences in derived dust temperature with respect to the characteristic temperature of 20 K do not account for this difference. The mass ratios with the largest deviations from 1.0 are for those sources with $\alpha \ll 2$ or $\alpha > 3$, and indicate that the largest uncertainties in the mass estimates are from variations in the dust opacity. We investigate variations in the mass ratio with respect to source and stellar host characteristics in Section 4.

Almost two-thirds (63 per cent) of the sources were not detected at the 3σ level or above. The mean and standard error of mass for these sources, calculated using the mean of fluxes for sources not detected at the 3σ level, reported in Table 1, and using a dust temperature of 20 K, is $1.07 \pm 0.12 \times 10^{-3}$ $M_{\odot}$. We have a similar number of non-detections for the Class II and Class III sources, which have mean and standard errors of $1.26 \pm 0.21 \times 10^{-3}$ and $0.83 \pm 0.06 \times 10^{-3}$ $M_{\odot}$. We investigate further the mass limits and structure of non-detections in Section 3.2. Of the five Class II sources characterized as probable transition discs, we detect one, the multiple source FO Tau A and B, and calculate a disc mass of 0.86×10^{-3} $M_{\odot}$. Multiplicity in disc sources hampers efforts to characterize their physical characteristics (Najita et al. 2007), which we investigate in Section 4.

3.2 Source characteristics by class

The detection rate for our disc sample decreases with evolutionary class. For example, at 850 μm, there is only one non-detection for the eight Class I sources, but only two detections for the nineteen Class III sources. The wide-field mapping available with the SCUBA-2 data sets means that we can investigate in a statistical manner the material surrounding each of the disc sources. By stacking the data at the nominal disc positions, we can compare average properties by class.

Figs 6–8 show the stacked images at 850 μm (left) and 450 μm (right), with no local background subtracted. Also shown are the

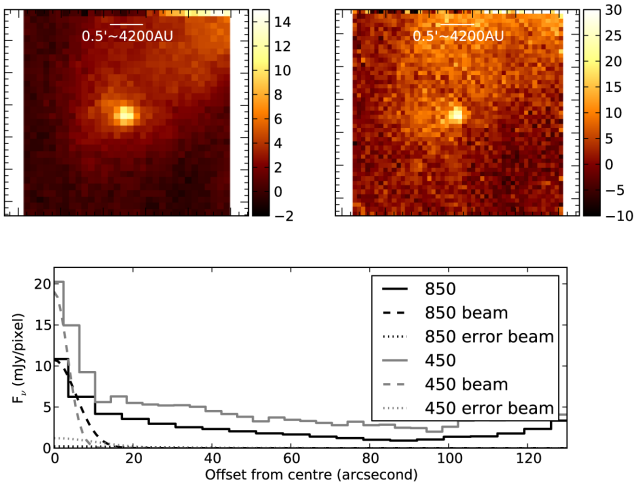

Figure 6. Top: stacked image of detected Class I sources at 850 μm (left) and 450 μm (right), with flux shown in mJy pixel^{-1}. Bottom: radially averaged emission profiles for the stacked images, showing the low-level extended emission in which the compact disc is embedded. Also shown are the relative contributions of the primary and secondary (error) beams at each wavelength. Using a two-component Gaussian fit to model the radial profiles, the extended emission will contribute 30 per cent to the observed flux if not removed through background-subtracted aperture photometry.

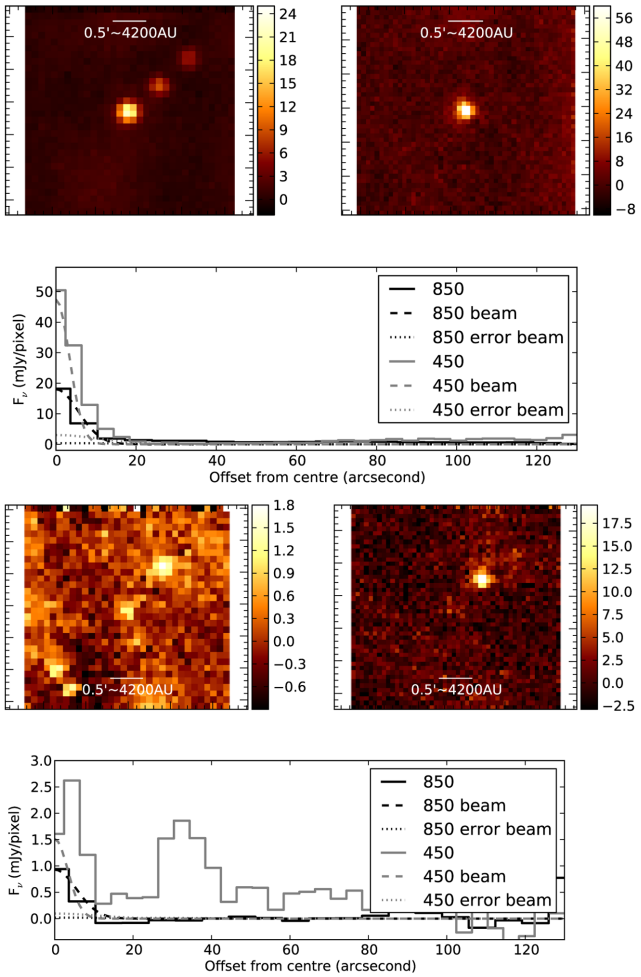

Figure 7. As Fig. 6 for detected (top) and non-detected (bottom) Class II sources. In addition to the disc source at the central position, nearby disc sources, bright enough to appear in the stacked image, are also seen, but are clearly separated from the nominal disc position.

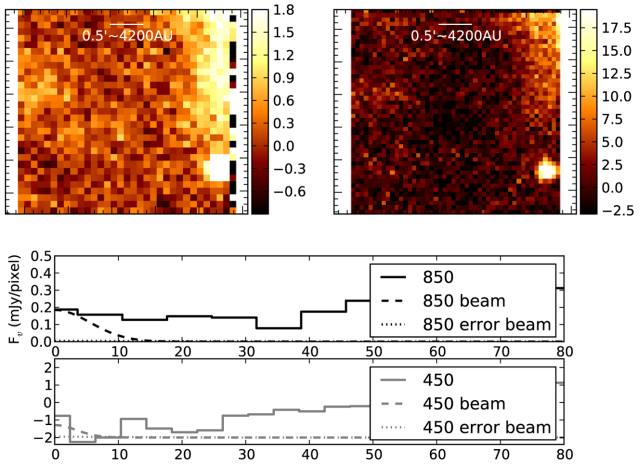

Figure 8. As Fig. 6 for non-detected Class III sources, with the radial profiles shown separately for each wavelength. Bright nearby sources have been removed from the stacked data (see text).

radially averaged emission profiles over the central 2 arcmin of the stacked image and the relative contributions of the primary and secondary (error) beams at each wavelength.

Fig. 6 shows the stacked images and radially averaged emission profiles for the detected Class I sources. At both wavelengths, we see compact emission peaks within extended low-level emission. The apertures used to measure background-subtracted fluxes for these disc sources, with a diameter of 20 arcsec and local background measured in annuli of 30–40 arcsec, probe size scales of 2800–5600 au, and should reduce contamination in the observed disc flux due to emission from the envelope, which could extend to scales ∼20 000 au. A two-component Gaussian fit to the radial profiles indicates that the low-level wide component – associated with the envelope – will contribute 30 per cent to the fluxes at both wavelengths if not removed. The compact peak can be associated with an unresolved disc, with widths of 6.3–7.7 arcsec (∼1000 au). At SCUBA-2's resolutions, we are not able to resolve any accretion disc that might be present.

For the Class II sources, we can compare the structure of detected and non-detected sources using stacked data, shown in Fig. 7. Nearby compact sources are bright enough to be seen in the Class II stacked data for detections and non-detections, but are clearly separated from the nominal disc positions. For the detected and non-detected sources at both wavelengths, the compact peak has a width of 6.37.0 arcsec (∼1000 au). At 450 μm, the stacked data for non-detections show a weak central peak, which is offset by just a few arcseconds from the nominal central position, making it difficult to determine the contribution to the measured disc flux. This offset may indicate dust asymmetry in the disc, suggesting that the non-detected Class II discs are more evolved, rather than just less luminous. At 850 μm, and for detected 450 μm sources, the narrow component contributes at least 95 per cent of the flux.

The stacked data for the Class III sources are dominated by extended arcs of emission at offsets of ∼1 arcmin from the nominal central position, which arise in a small number of sources located near the strongest emission in the map, the bright reflection nebula illuminated by the Class II Ae star V892 Tau. These sources (V410 Tau and V410 X-Ray 3 undetected at both wavelengths, V410 X-Ray 4 and V410 Anon 25 undetected at 450 μm) have been removed from the final stacked data, shown in Fig. 8. Extended emission at distances >1 arcmin from the disc position remains in the stacked data, however. The emission decreases radially towards the disc position, and at offsets <0.5 arcmin from the disc position, the flux is more consistent with a flat profile, particularly at 850 μm. There may be emission from the central 6–10 arcsec region, but higher sensitivity data are required to investigate whether or not the dust 'hole' for these sources is real.

With the discs in both Class I and Class II sources unresolved at this resolution, we are unable to determine differences in observable disc size at submillimetre wavelengths between the classes. The differences in emission structure that we do observe are instead dominated by envelope and/or cloud material. The derived physical characteristics show only small differences on average between Class I and Class II objects, with those in each phase covering similar ranges in temperature, α and disc mass. In the next ection, we investigate alternative indicators of disc evolution.

4 DISC EVOLUTION

Disc masses are known to decline with age, and to be intrinsically lower for late-type stellar hosts. Andrews et al. (2013) have shown that the disc luminosity and mass are correlated with stellar host mass for Class II sources, with more massive stars more likely to have more massive discs. In this section, we investigate this correlation for M- and K-spectral-type Class I and Class II sources in L 1495.

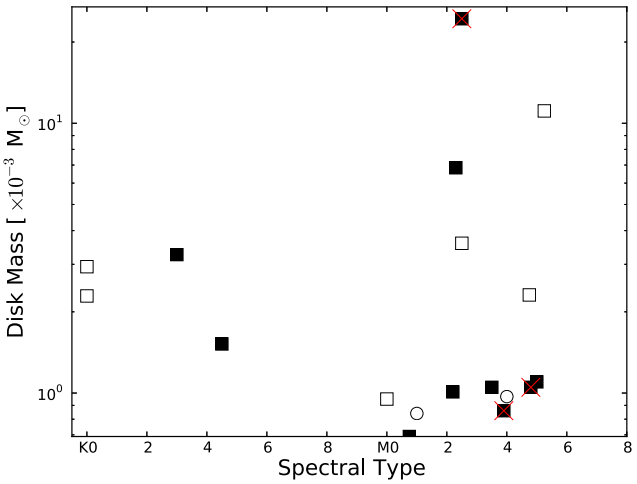

Figure 9. Disc mass (at 20 K) as a function of spectral type for Class I (open squares), Class II (closed squares) and Class III (open circles). Red crosses mark known multiple sources.

A wide variety of stellar masses have been computed from spectral types of young, PMS stars, and to date it is been difficult to determine dynamical stellar masses (Schaefer et al. 2009). We therefore use stellar types as a proxy for stellar mass, to minimize the assumptions made about stellar hosts. For Class I sources with a range of possible spectral types, the median value has been used.

Fig. 9 shows the disc mass, calculated assuming a dust temperature of 20 K, as a function of spectral type. Since binary or higher multiple disc sources may have multiple and/or circumbinary discs, we identify known binaries in the plot. The multiple sources all have late spectral types, and with the exception of MHO1/2, are at the lower end of the mass distribution. For both Classes, M-type stellar hosts have a wider distribution of disc mass than K-type stellar hosts, with stellar hosts of spectral types M2 to M6 having the largest range of mass. For the Class II sources, with the exception of the anomalous CY Tau and multiple MHO1/2 sources, M-type stellar hosts have lower masses than K-type stellar hosts. These data support results from studies of late spectral-type PMS stars in Taurus at high resolution, which have similarly found evidence that disc masses decrease over the limited spectral range of K–M stars, with a difference in flux observed at the M2–M3 spectral type (Schaefer et al. 2009) and $M_{\rm d} \propto M_{\star}$ in a linear scaling (Andrews et al. 2013).

Fig. 9 shows a slight trend in the opposite direction for the Class I disc sources, with later spectral types extending to larger masses, which may be associated with a difference in evolutionary timescales for more massive stellar hosts. Given the difficulty in determining spectral types for Class I sources, however, this trend is much less clearly defined than for the Class II sources.

Fig. 10 shows the disc mass derived at each wavelength, calculated assuming $T_{\rm dust} = 20$ K, with source class and multiple sources marked as in Fig. 9. Additionally, magenta circles and cyan triangles mark discs with stellar hosts of spectral type M and K, respectively. Discs with stellar hosts of spectral type K consistently have higher 450-μm disc masses than 850-μm disc masses. For discs with stellar hosts of spectral type M, and for the different disc classes, there are no clear trends in the mass ratio. Although variations in dust opacity are the largest source of uncertainty in disc mass calculations, these

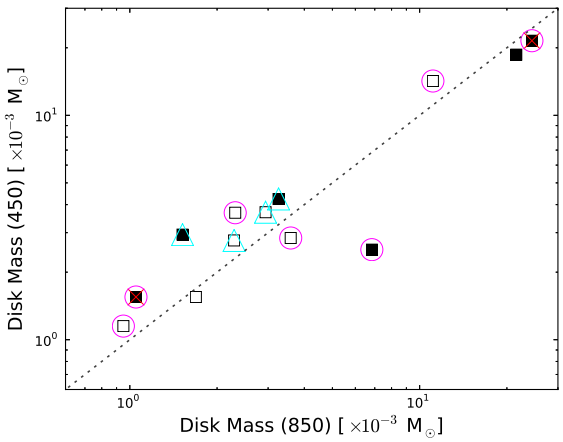

Figure 10. Disc mass (at 20 K) calculated from 850 μm flux against that calculated from 450 μm flux. Disc class and multiple sources as in Fig. 9, with magenta circles and cyan triangles marking discs of spectral type M and K, respectively. The dotted line shows the 1:1 ratio.

results suggest that there could be an intrinsic difference in the dust opacity, or the dust temperature, or a combination of both, for discs surrounding K-type stellar hosts compared to those surrounding M-type stellar hosts. Earlier type stars have higher luminosities, which generally leads to higher dust temperatures in the disc (Andrews et al. 2013). Once complete, the full GBS data set will provide a much larger sample with which to investigate this difference.

5 CONCLUSIONS

(i) CO contamination in the continuum at 850 μm is negligible in L 1495, with only five sources showing contamination levels over 5 per cent, all of which are below 15 per cent.

(ii) Across the L 1495 region, the spectral slope $\alpha = 2.8 \pm 0.6$, suggesting that much of the dust detected by SCUBA-2 has undergone grain growth.

(iii) Class I and Class II discs have similar distributions of α values, with four sources having $2.5 < \alpha < 3$, and eight sources with $1.4 < \alpha < 2.5$. These results imply that $\beta \simeq 1$ for the majority of disc sources, but that both classes show evidence either for small, optically thick discs, or rapid grain growth.

(iv) Class I sources have slightly higher dust colour temperatures than Class II sources, although both classes have similar ranges of dust temperature, 7–40 K. In two Class I sources (IRAS 04108+2803A and IRAS 04108+2803B) the 450/850-μm flux ratio is approaching the upper limit of 50 K, where the dust colour temperature is unconstrained, particularly for low β values.

(v) In L 1495, 2/29 Class II sources have disc masses $M_{\rm d} > 20\ M_{\rm JUP}$. If masses are calculated from the dust colour temperature, then the two coldest sources have much larger masses i.e. 3/29 Class II sources and 1/8 Class I sources have $M_{\rm d} > 20\ M_{\rm JUP}$.

(vi) We detect a higher percentage of discs with stellar hosts of spectral type K than those of spectral type M, with detection rates of 50 and 33 per cent, respectively, at 850 μm. At 450μm, we detect the same 50 per cent of objects with stellar hosts of spectral type K, but only 16 per cent of those of spectral type M. Variations in the dust opacity lead to the largest uncertainties in disc mass calculations, but our results suggest there is an intrinsic difference in the dust opacity, and/or the dust opacity between discs with stellar hosts of spectral type M and K. The latter all have higher disc masses calculated using 450 μm fluxes than calculated using 850 μm data.

The Legacy data sets forming the JCMT GBS will be used to extend this analysis across a range of star-forming regions, so that comparisons between regions and star-forming environments can be made.

The largest uncertainty in calculating disc masses is in determining the dust opacity, particularly for observations where the discs are not resolved. Research in this field will make significant progress when the full capabilities of ALMA become available, and nearby discs can be imaged at millimetre/submillimetre wavelengths on scales of a few au.

ACKNOWLEDGEMENTS

The JCMT is operated by the Joint Astronomy Centre on behalf of the Science and Technology Facilities Council of the UK, the National Research Council of Canada and (until 2013 March 31) the Netherlands Organisation for Scientific Research. Additional funds for the construction of SCUBA-2 were provided by the Canada Foundation for Innovation. DJ is supported by the National Research Council of Canada and by a Natural Sciences and Engineering Research Council of Canada (NSERC) Discovery Grant. This publication makes use of data products from the Two Micron All Sky Survey, which is a joint project of the University of Massachusetts and the Infrared Processing and Analysis Center/California Institute of Technology, funded by the National Aeronautics and Space Administration and the National Science Foundation.

REFERENCES

Adams F. C., Lada C. J., Shu F. H., 1987, ApJ, 312, 788
Akeson R. L., Jensen E. L. N., 2014, ApJ, 784, 62
Andrews S. M., Williams J. P., 2005, ApJ, 631, 1134
Andrews S. M., Rosenfeld K. A., Kraus A. L., Wilner D. J., 2013, ApJ, 771, 129
Beckwith S. V. W., Sargent A. I., Chini R. S., Güsten R., 1990, AJ, 99, 924
Buckle J. V. et al., 2009, MNRAS, 399, 1026
Chapin E. L., Berry D. S., Gibb A. G., Jenness T., Scott D., Tilanus R. P. J., Economou F., Holland W. S., 2013, MNRAS, 430, 254
Crapsi A., van Dishoeck E. F., Hogerhiejde M. R., Pontoppodan K. M., Dullemond C. P., 2008, A&A, 486, 245
Cutri et al., 2003, VizieR On-line Data Catalogue: II/246, 2246, 0
Cutri et al., 2014, VizieR On-line Data Catalogue: II/328, 2328, 0
Davis S., 2005, ApJ, 627, L153
Davis C. J. et al., 2010, MNRAS, 405, 759
Dempsey J. T. et al., 2013, MNRAS, 430, 2534
Dodds P., Greaves J. S., Scholz A., Hatchell J., Holland W. S., The JCMT Gould Belt Survey Team, 2015, MNRAS, 447, 722
Drabek E. et al., 2012, MNRAS, 426, 23
Elias J. H., 1978, ApJ, 224, 857
Esplin T. L., Luhman K. L., Mamajek E. E., 2014, ApJ, 784, 126
Evans N. J. et al., 2009, ApJS, 181, 321
Furlan E. et al., 2011, ApJS, 195, 3
Gomez M., Hartmann L., Kenyon S. J., Hewett R., 1993, AJ, 105, 1927
Güdel M., Padgett D. L., Dougados C., 2007, in Reipurth B., Jewitt D., Keil K., eds, Protostars and Planets V. Univ. Arizona Press, Tucson, AZ, p. 329
Guilloteau S., Somin M., Piétu V., Di Folco E., Dutrey A., Prato L., Chapillon E., 2014, A&A, 567, 117
Hatchell J et al., 2013, MNRAS, 429, L10
Herczeg G. J., Hillenbrand L. A., 2014, ApJ, 786, 32
Hernández J. et al., 2007, ApJ, 662, 1067
Holland W. S., Bintley D., Chapin E. L., 2013, MNRAS, 430, 2513
Kenyou S. J., Hartmann L., 1995, ApJS, 101, 117
Lada C. J., 1987, in Peimbert M., Jugaka J., eds, Proc. IAU Symp. 115, Star Forming Regions. Reidel, Dordrecht, p. 1
Lee N., Williams J. P., Cieza L. A., 2011, ApJ, 736, 135

Luhman K. L., Allen P. R., Espaillat C., Hartmann L., Calvet N., 2010, ApJS, 186, 111
Mohanty S. et al., 2013, ApJ, 773, 168
Najita J. R., Strom S. E., Muzerolle J., 2007, MNRAS, 387, 369
Pecaut M. J., Mamajek E. E., 2013, ApJS, 208, 9
Redbull L. M. et al., 2010, ApJS, 186, 259
Ricci L., Testi L., Natta A., Neri R., Cabrit S., Herczeg G. J., 2010, A&A, 512, 15
Robitaille T. P., Whitney B. A., Indebedtouw R., Wook K., 2007, ApJS, 169, 328
Roeser S., Schilbach E., Schwan H., Kharchenko N. V., Piskunov A. E., Scholz R.-D., 2008, A&A, 488, 401
Sadavoy S. I. et al., 2013, ApJ, 767, 126
Salji C., Richer J., Buckle J. V. et al., 2014, MNRAS, submitted
Schaefer G. H., Dutry A., Guilloteau S., Simon M., White R. J., 2009, ApJ, 701, 698
Ward-Thompson D. et al., 2007, PASP, 119, 855
Whitney B. A., Wood K., Bjorkman J. E., Wolff M. J., 2003, ApJ, 591, 1049
Williams J. P., Cieza L. A., 2011, ARA&A, 49, 67
Williams J. P. et al., 2013, MNRAS, 435, 1671

APPENDIX A: DISC CONTINUUM IMAGES

Figs A1–A56 show thumbnail images of the dust continuum at the nominal position for each disc at 850 and 450 μm. The flux is shown in mJy pixel^{-1}, and circles show the 20 arcsec aperture used to measure fluxes. The centrally aligned source is the one named in the caption.

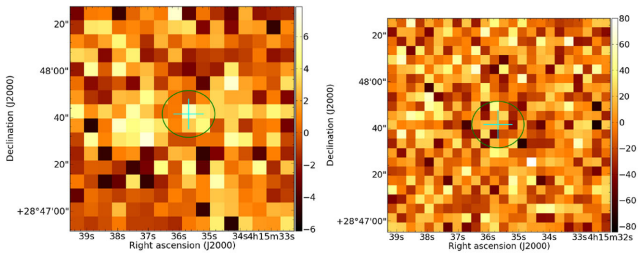

Figure A1. 850-μm (left) and 450-μm (right) dust continuum towards J04153566+2847417 Class I.

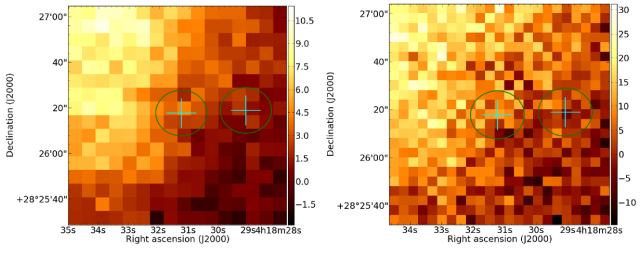

Figure A2. As Fig. A1 SSTTau041831.2+28261 Class I.

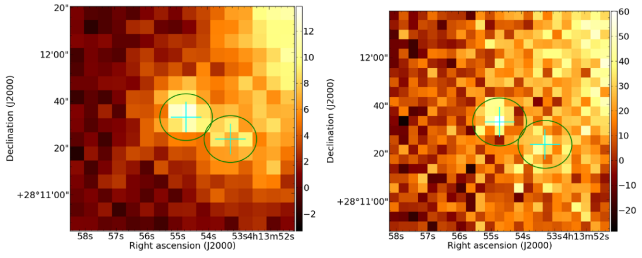

Figure A3. As Fig. A1 IRAS 04108+2803B Class I.

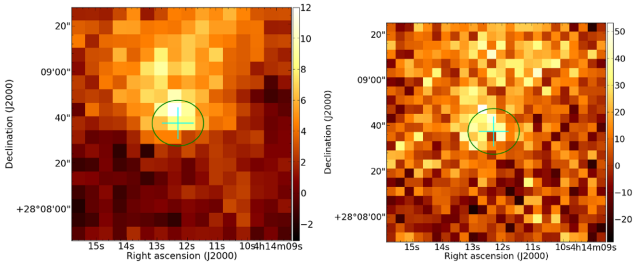

Figure A4. As Fig. A1 IRAS 04111+2800G Class I.

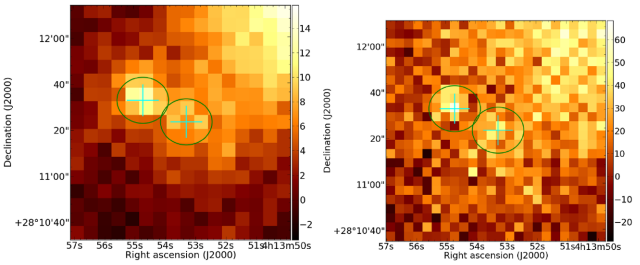

Figure A5. As Fig. A1 IRAS 04108+2803A Class I.

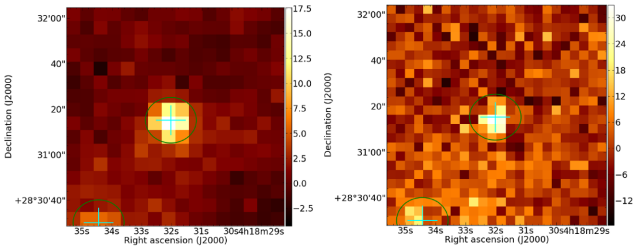

Figure A6. As Fig. A1 IRAS 04154+2823 Class I.

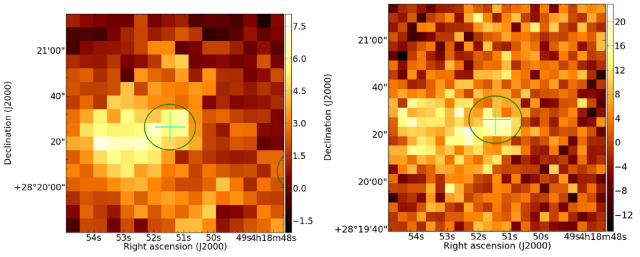

Figure A7. As Fig. A1 CoKuTau/1 Class I.

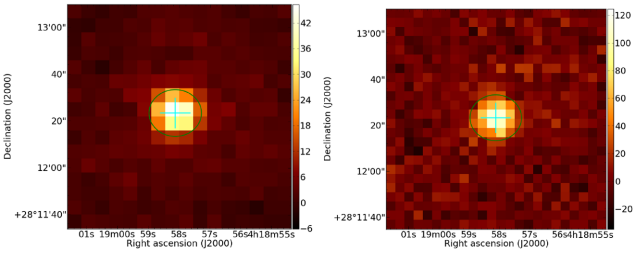

Figure A8. As Fig. A1 IRAS 04158+2805 Class I.

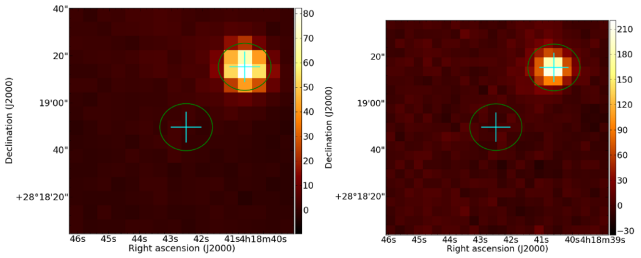

Figure A9. As Fig. A1 V410X-ray7 Class II.

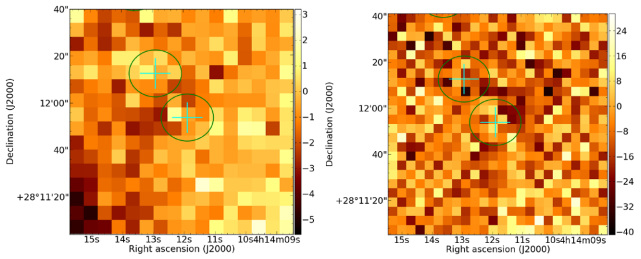

Figure A10. As Fig. A1 J04141188+2811535 Class II.

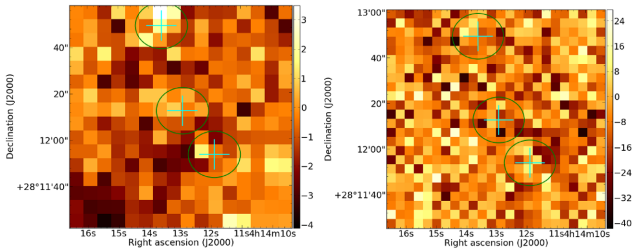

Figure A11. As Fig. A1 V773TauA+B Class II.

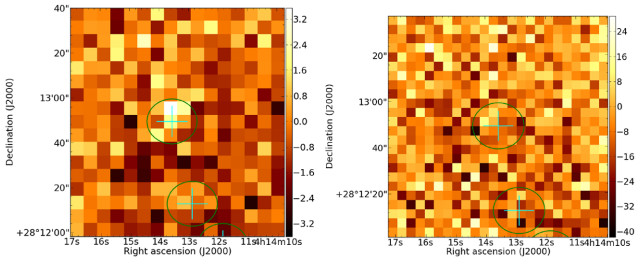

Figure A12. As Fig. A1 FMTau Class II.

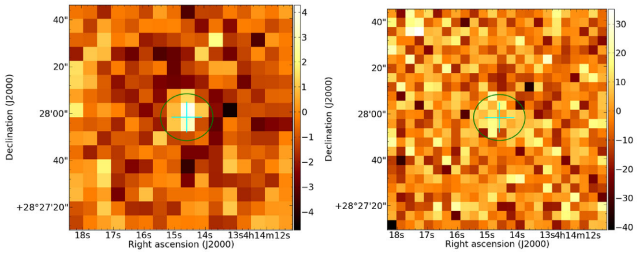

Figure A13. As Fig. A1 FNTau Class II.

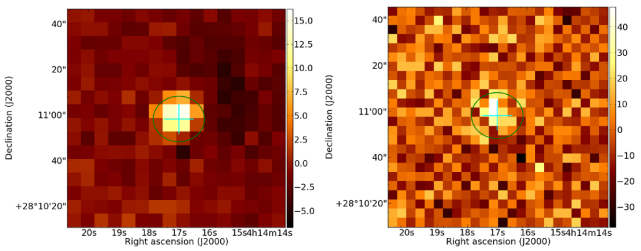

Figure A14. As Fig. A1 CWTau Class II.

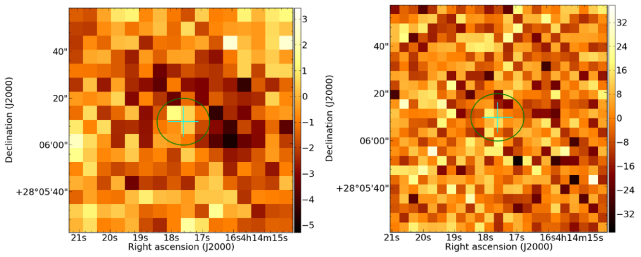

Figure A15. As Fig. A1 CIDA1 Class II.

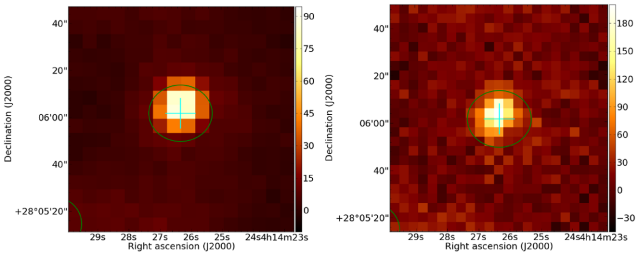

Figure A16. As Fig. A1 MHO1/2 Class II. A larger 24 arcsec aperture was used for this source..

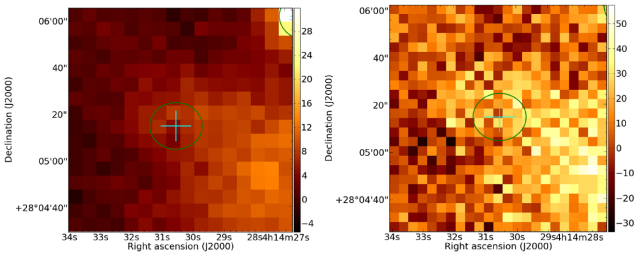

Figure A17. As Fig. A1 MHO3 Class II.

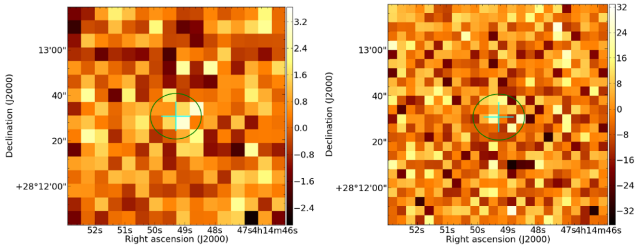

Figure A18. As Fig. A1 FOTauA+B Class II.

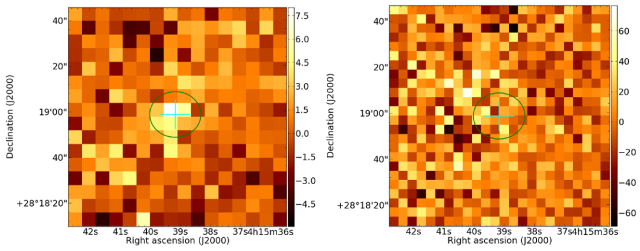

Figure A19. As Fig. A1 J04153916+2818586 Class II.

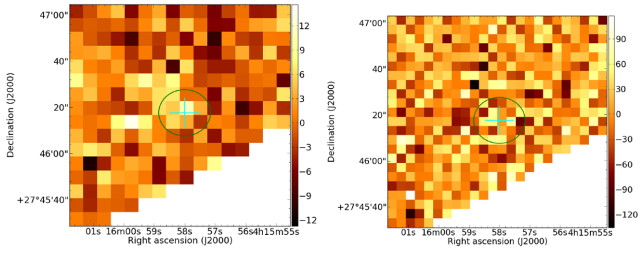

Figure A20. As Fig. A1 J04155799+2746175 Class II.

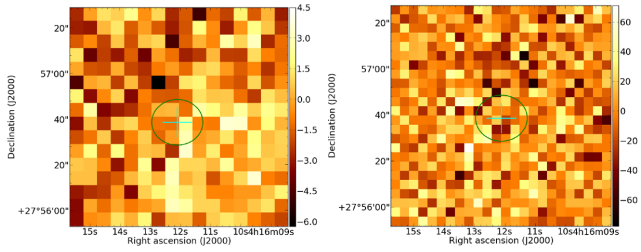

Figure A21. As Fig. A1 J04161210+2756385 Class II.

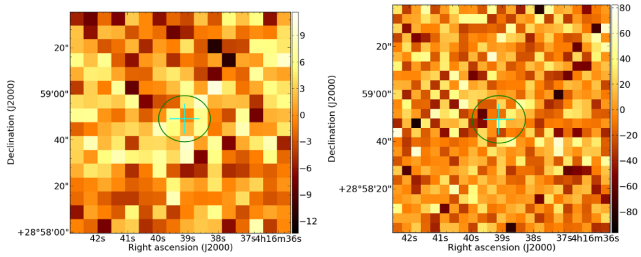

Figure A22. As Fig. A1 J04163911+2858491 Class II.

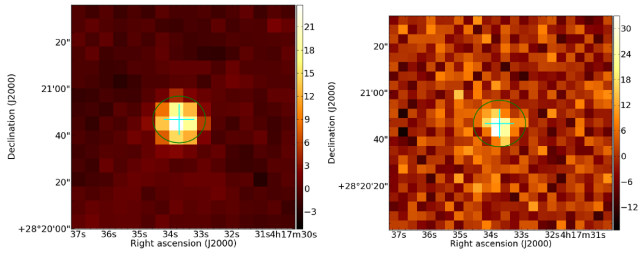

Figure A23. As Fig. A1 CYTau Class II.

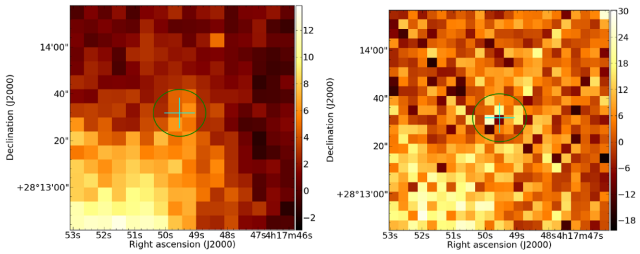

Figure A24. As Fig. A1 KPNO10 Class II.

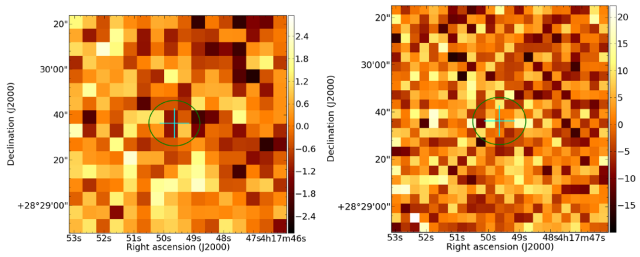

Figure A25. As Fig. A1 V410X-ray1 Class II.

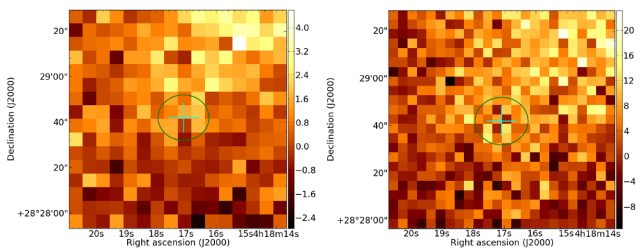

Figure A26. As Fig. A1 V410Anon13 Class II.

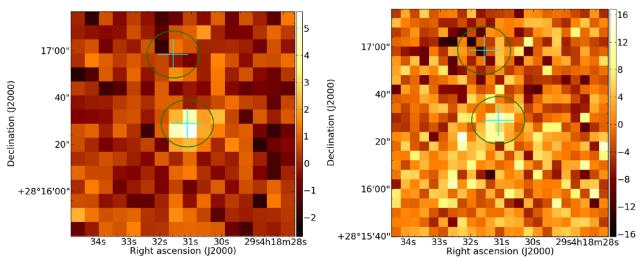

Figure A27. As Fig. A1 DDTauA+B Class II.

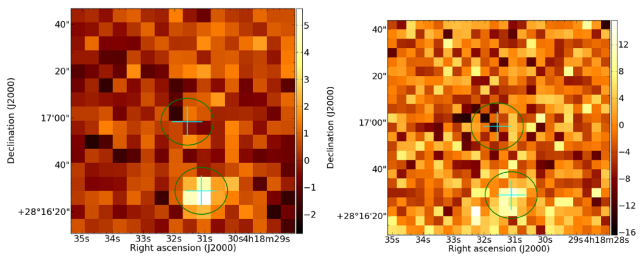

Figure A28. As Fig. A1 CZTauA+B Class II.

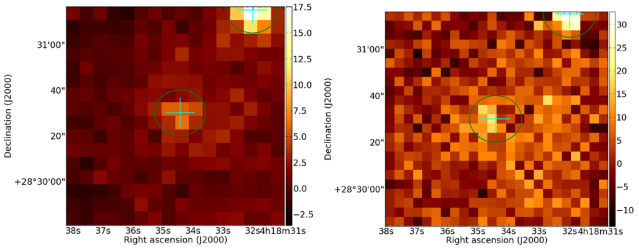

Figure A29. As Fig. A1 V410X-ray2 Class II.

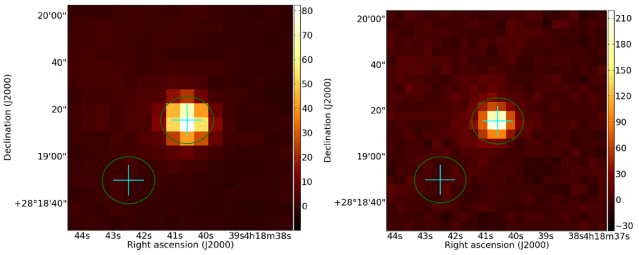

Figure A30. As Fig. A1 V892Tau Class II.

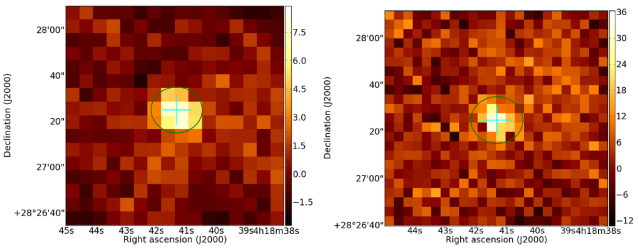

Figure A31. As Fig. A1 LR1 Class II.

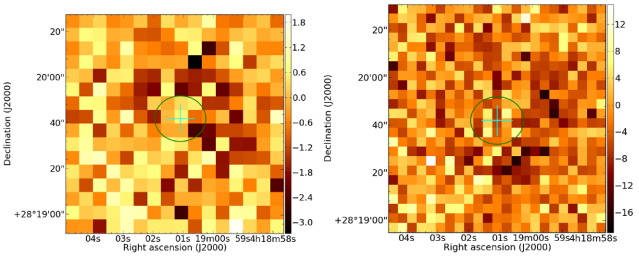

Figure A32. As Fig. A1 V410X-ray6 Class II.

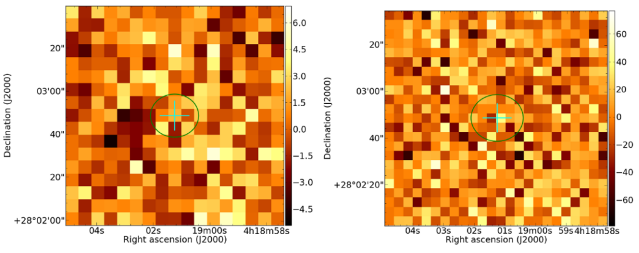

Figure A33. As Fig. A1 KPNO12 Class II.

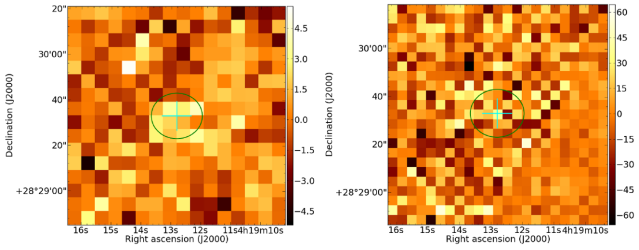

Figure A34. As Fig. A1 FQTauA+B Class II.

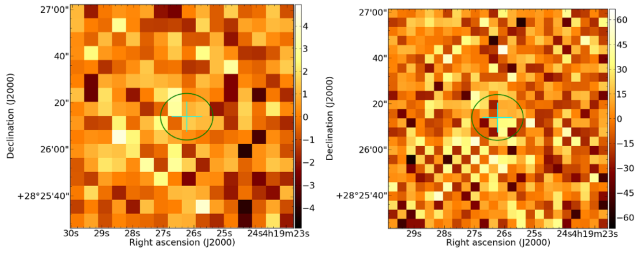

Figure A35. As Fig. A1 V819Tau Class II.

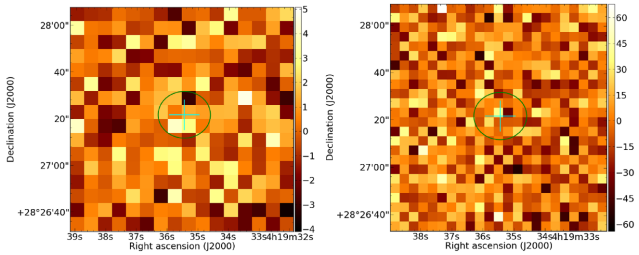

Figure A36. As Fig. A1 FRTau Class II.

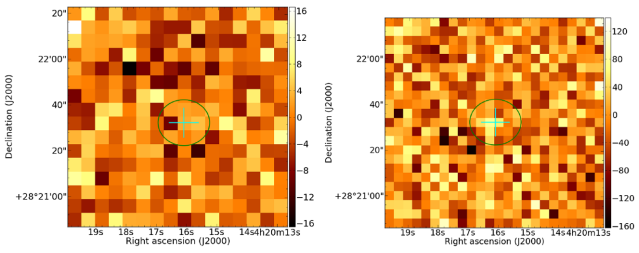

Figure A37. As Fig. A1 J04201611+2821325 Class II.

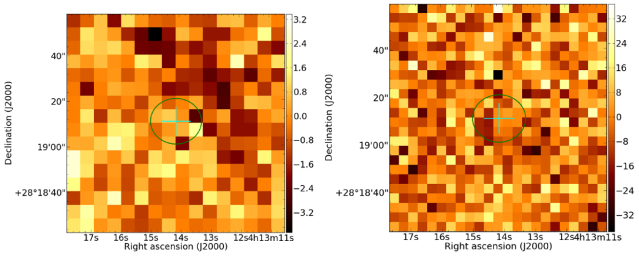

Figure A38. As Fig. A1 LkCa1 Class III.

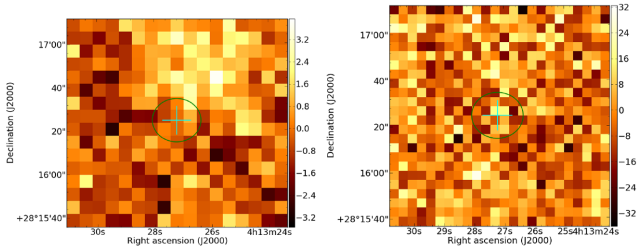

Figure A39. As Fig. A1 Anon1 Class III.

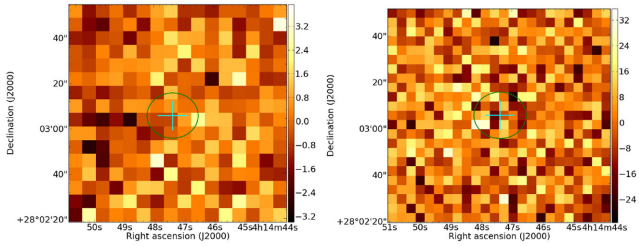

Figure A40. As Fig. A1 XEST20-066 Class III.

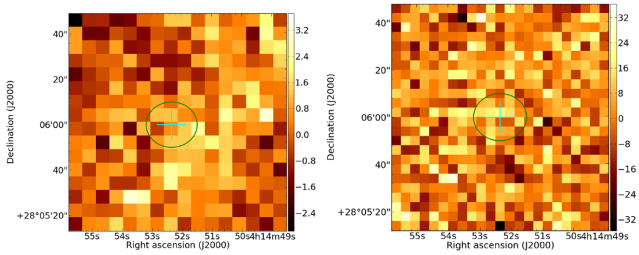

Figure A41. As Fig. A1 XEST20-071 Class III.

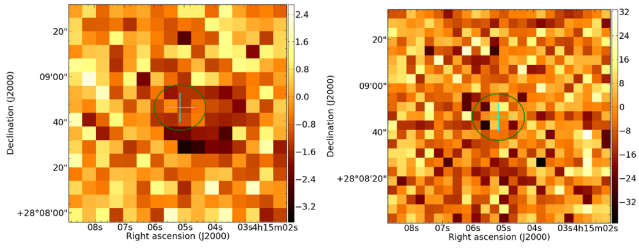

Figure A42. As Fig. A1 CIDA2 Class III.

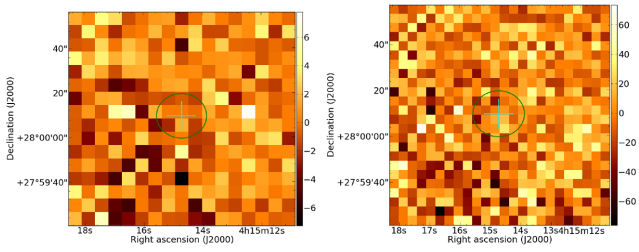

Figure A43. As Fig. A1 KPNO1 Class III.

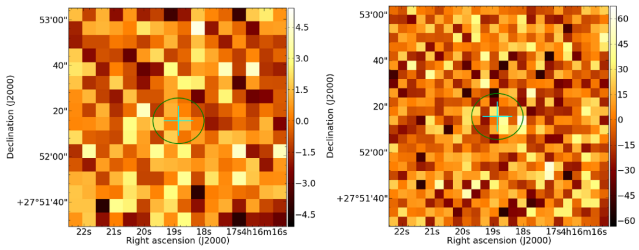

Figure A44. As Fig. A1 J04161885+2752155 Class III.

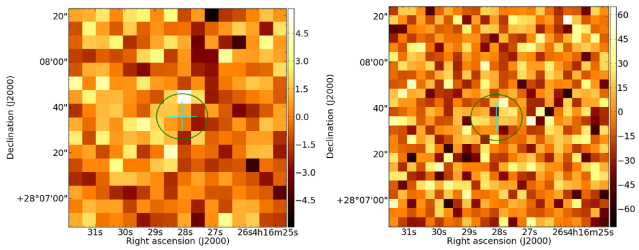

Figure A45. As Fig. A1 LkCa4 Class III.

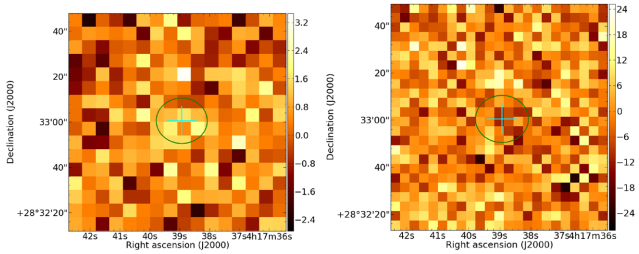

Figure A46. As Fig. A1 LkCa5 Class III.

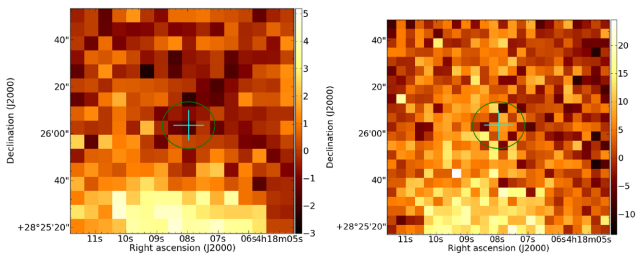

Figure A47. As Fig. A1 V410Xray3 Class III.

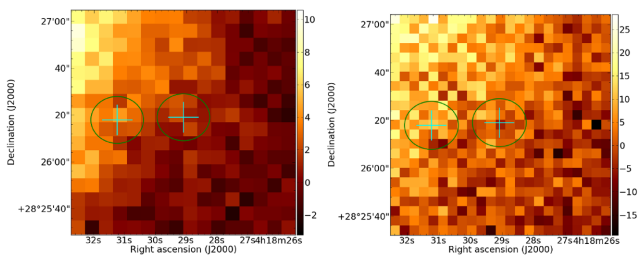

Figure A48. As Fig. A1 V410Anon25 Class III.

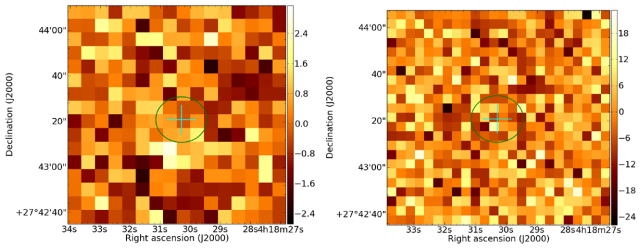

Figure A49. As Fig. A1 KPNO11 Class III.

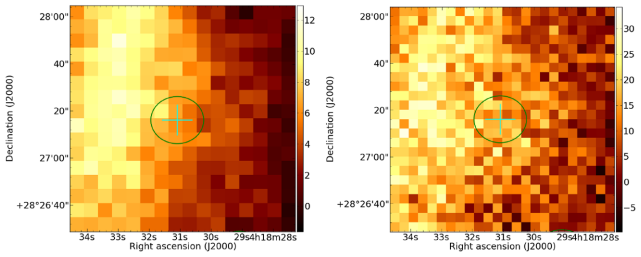

Figure A50. As Fig. A1 V410TauA+B+C Class III.

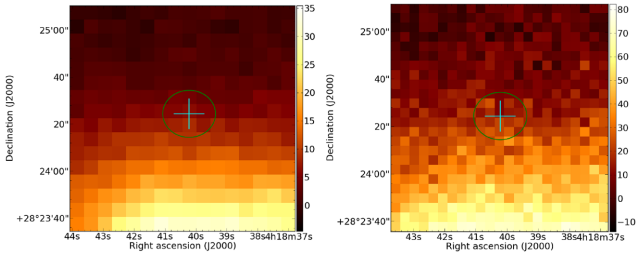

Figure A51. As Fig. A1 V410X-ray4 Class III.

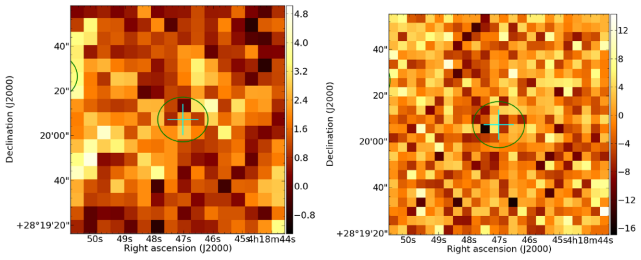

Figure A52. As Fig. A1 Hubble4 Class III.

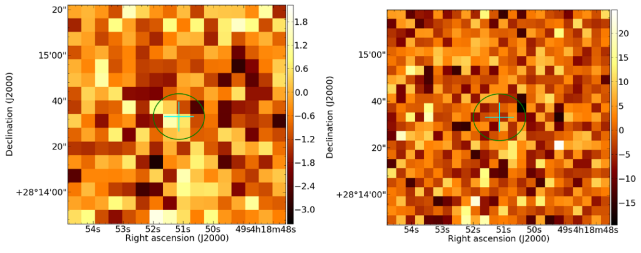

Figure A53. As Fig. A1 KPNO2 Class III.

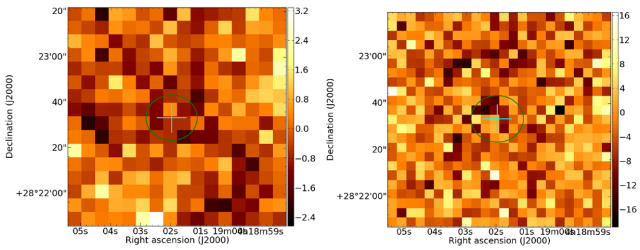

Figure A54. As Fig. A1 V410X-ray5a Class III.

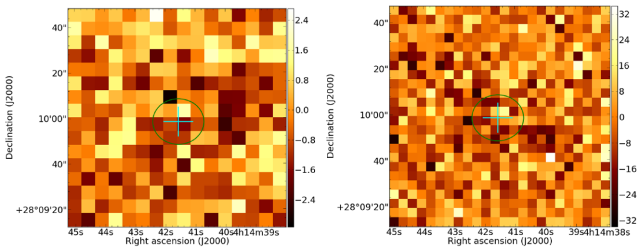

Figure A55. As Fig. A1 J04144158+2809583 Class III.

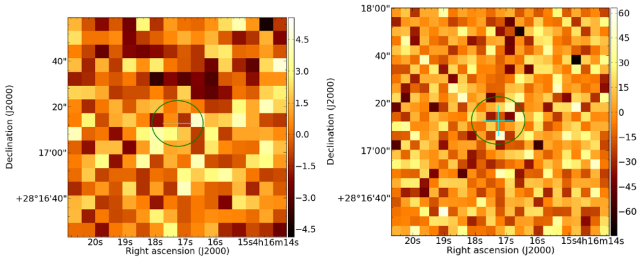

Figure A56. As Fig. A1 J04161726+2817128 Class III.

[1]*Astrophysics Group, Cavendish Laboratory, J J Thomson Avenue, Cambridge CB3 0HE, UK*
[2]*Kavli Institute for Cosmology, Institute of Astronomy, University of Cambridge, Madingley Road, Cambridge CB3 0HA, UK*
[3]*Imperial College London, Blackett Laboratory, Prince Consort Rd, London SW7 2BB, UK*
[4]*Physics & Astronomy, University of St Andrews, North Haugh, St Andrews, Fife KY16 9SS, UK*
[5]*NRC Herzberg Astronomy and Astrophysics, 5071 West Saanich Rd, Victoria, BC V9E 2E7, Canada*
[6]*Department of Physics and Astronomy, University of Victoria, Victoria, BC V8P 1A1, Canada*
[7]*Joint Astronomy Centre, 660 N. A'ohōkū Place, University Park, Hilo, Hawaii 96720, USA*
[8]*Department of Physics and Astronomy, University of Waterloo, Waterloo, ON N2L 3G1, Canada*
[9]*Physics and Astronomy, University of Exeter, Stocker Road, Exeter EX4 4QL, UK*
[10]*Department of Astronomy, Cornell University, Ithaca, NY 14853, USA*
[11]*Leiden Observatory, Leiden University, PO Box 9513, NL-2300 RA Leiden, the Netherlands*
[12]*School of Physics and Astronomy, Cardiff University, The Parade, Cardiff CF24 3AA, UK*
[13]*Jeremiah Horrocks Institute, University of Central Lancashire, Preston, Lancashire PR1 2HE, UK*
[14]*European Southern Observatory (ESO), D-85748 Garching bei München, Germany*

[15]*Jodrell Bank Centre for Astrophysics, Alan Turing Building, School of Physics and Astronomy, University of Manchester, Oxford Road, Manchester M13 9PL, UK*
[16]*Centre de Recherche en Astrophysique du Québec et département de physique, Université de Montréal, C.P. 6128, succ. centre-ville, Montréal, QC H3C 3J7, Canada*
[17]*James Madison University, Harrisonburg, Virginia 22807, USA*
[18]*School of Physics, Astronomy & Mathematics, University of Hertfordshire, College Lane, Hatfield, HERTS AL10 9AB, UK*
[19]*Astrophysics Research Institute, Liverpool John Moores University, Egerton Warf, Birkenhead CH41 1LD, UK*
[20]*Dunlap Institute for Astronomy & Astrophysics, University of Toronto, 50 St George St, Toronto, ON M5S 3H4, Canada*
[21]*Department of Physical Sciences, The Open University, Milton Keynes MK7 6AA, UK*
[22]*The Rutherford Appleton Laboratory, Chilton, Didcot OX11 0NL, UK*
[23]*UK Astronomy Technology Centre, Royal Observatory, Blackford Hill, Edinburgh EH9 3HJ, UK*
[24]*Institute for Astronomy, Royal Observatory, University of Edinburgh, Blackford Hill, Edinburgh EH9 3HJ, UK*
[25]*Centre de recherche en astrophysique du Québec et Département de physique, de génie physique et d'optique, Université Laval, 1045 avenue de la médecine, QC G1V 0A6, Canada*
[26]*Department of Physics and Astronomy, UCL, Gower St, London WC1E 6BT, UK*
[27]*Department of Physics, University of Alberta, Edmonton, AB T6G 2E1, Canada*
[28]*Max Planck Institute for Astronomy, Königstuhl 17, D-69117 Heidelberg, Germany*
[29]*University of Western Sydney, Locked Bag 1797, Penrith, NSW 2751, Australia*
[30]*Department of Physics and Astronomy, University College London, Gower Street, London WC1E 6BT, UK*
[31]*Department of Physics and Astronomy, McMaster University, Hamilton, ON L8S 4M1, Canada*
[32]*National Astronomical Observatory of China, 20A Datun Road, Chaoyang District, Beijing 100012, China*

This paper has been typeset from a TEX/LATEX file prepared by the author.